DRAFT VERSION JANUARY 13, 2022
Typeset using LaTeX **twocolumn** style in AASTeX63

Three-Dimensional Hydrodynamic Simulations of Convective Nuclear Burning In Massive Stars Near Iron Core Collapse

C. E. FIELDS [1,2,3,*] AND SEAN M. COUCH [4,5,6]

[1] *Center for Theoretical Astrophysics, Los Alamos National Laboratory, Los Alamos, NM 87545, USA*
[2] *Computer, Computational, and Statistical Sciences Division, Los Alamos National Laboratory, Los Alamos, NM 87545, USA*
[3] *X Computational Physics Division, Los Alamos National Laboratory, Los Alamos, NM 87545, USA*
[4] *Department of Physics and Astronomy, Michigan State University, East Lansing, MI 48824, USA*
[5] *Department of Computational Mathematics, Science, and Engineering, Michigan State University, East Lansing, MI 48824, USA*
[6] *Facility for Rare Isotope Beams, Michigan State University, East Lansing, MI 48824, USA*

Submitted to ApJ

ABSTRACT

Non-spherical structure in massive stars at the point of iron core collapse can have a qualitative impact on the properties of the ensuing core-collapse supernova explosions and the multi-messenger signals they produce. Strong perturbations can aid successful explosions by strengthening turbulence in the post-shock region. Here, we report on a set of 4π 3D hydrodynamic simulations of O- and Si-shell burning in massive star models of varied initial masses using MESA and the FLASH simulation framework. We evolve four separate 3D models for roughly the final ten minutes prior to, and including, iron core collapse. We consider initial 1D MESA models with masses of 14-, 20-, and 25 $M_\odot$ to survey a range of O/Si shell density and compositional configurations. We characterize the convective shells in our 3D models and compare them to the corresponding 1D models. In general, we find that the angle-average convective speeds in our 3D simulations near collapse are *three* to *four* times larger than the convective speeds predicted by MESA at the same epoch for our chosen mixing length parameter of $\alpha_{\rm MLT} = 1.5$. In three of our simulations, we observe significant power in the spherical harmonic decomposition of the radial velocity field at harmonic indices of $\ell = 1-3$ near collapse. Our results suggest that large-scale modes are common in massive stars near collapse and should be considered a key aspect of pre-supernova progenitor models.

Keywords: Stellar convective zones (301), Hydrodynamics (1963), Late stellar evolution (911), Massive stars (732), Supernovae (1668)

1. INTRODUCTION

Three-dimensional (3D) simulations of core-collapse supernova (CCSN) explosions have benefitted from imposing pre-supernova velocity perturbations that aim to replicate nuclear burning in Si- and O-shell convective regions. The inclusion of these perturbations were shown to lead to larger non-radial kinetic energy in the gain region providing turbulent pressure behind the stalled shock capable of driving explosion in a model that otherwise failed to explode without perturbations (Couch & Ott 2013). In the work of O'Connor & Couch (2018a), they impose perturbations in the 3D CCSN explosion of a 20 $M_\odot$ model (Farmer et al. 2016). Their 3D perturbed CCSN models evolved closer towards shock runaway and explosion but they did not observe shock runaway in any of the eight 3D simulations performed. The pre-supernova perturbations in the Si-shell region lead to an increase in the gravitational wave (GW) amplitude at $t_{\rm pb} \approx 200$ ms over a frequency band of 200 - 1000 Hz. This result suggests that convective perturbations can also lead to qualitative differences in the multi-messenger signals produced in CCSN simulations.

Work by Couch et al. (2015) presented the results of a 3D CCSN progenitor model evolved for the final ≈ 155 s prior to and including iron core-collapse. Using this 3D progenitor model they performed two CCSN explosion simulations

Corresponding author: C. E. Fields
carlnotsagan@lanl.gov

* RPF Distinguished Fellow

using the 3D progenitor model and a 1D angle-average of the 3D model. They found that increased turbulent motions in the post shock region in the 3D progenitor explosion model can aid in successful explosion. This model also showed a slight increase in turbulent kinetic energy in the gain region, a similar result to the CCSN models with artificial perturbations in Couch & Ott (2013). More recently, Müller et al. (2017) used the 18 $M_\odot$ 4π 3D progenitor of Müller et al. (2016) to perform three 3D CCSN explosion models. In their 3D explosion model using a 3D progenitor they found an increasing diagnostic explosion energy and baryonic mass of the PNS values closer agreement with those expected from observations (Pejcha & Thompson 2015). The two additional CCSN explosion models in their study - one a reduced velocity field 3D progenitor and the other a 1D angle-average initial model were less energetic and the 1D progenitor model failed to explode. The results of this study suggest that 3D progenitors can aide in closing the gap between low explosion energy and PNS properties predicted by other works using 1D progenitors (Burrows et al. 2020).

Multidimensional CCSN progenitor models have been performed recently (Müller et al. 2016; Yoshida et al. 2019; Fields & Couch 2020; Yadav et al. 2019; Yoshida et al. 2021). Many of these simulations show convective properties that suggest favorable impact on the neutrino-driven CCSN explosion mechanism. In Yadav et al. (2019) they observe large-scale mixing due to merger of the O- and Ne-shells, a results which lead to large radial mach numbers in the merged shell regions. Despite this progress, it is expected that the convective properties in massive star will span a range of strength and flow dynamics over the initial mass range for CCSNe (Müller & Janka 2015). Currently, only a handful of 3D simulations sample this mass range and provide predictions for the Si- and O-shell convective properties of 3D massive star models.

In this Paper, we build on previous efforts exploring 3D progenitor models in the moments prior to collapse. We perform a total of four 4π 3D hydrodynamic simulations of Si- and O-shell burning for up to the final ten minutes prior to and including gravitational instability and iron core-collapse. We evolve models of initial $M_{\rm ZAMS}$ =14-, 20, and 25 $M_\odot$ using the FLASH simulation framework and the 1D stellar evolution code, MESA (Fryxell et al. 2000; Paxton et al. 2011, 2013, 2015, 2018). This work is novel because: (1) - we present four 3D long-term hydrodynamic simulations of O/Si shell burning in multiple progenitors, (2) - we investigate the impact of initial perturbations in pre-supernova hydrodynamic simulations in two 3D simulations of a 20 $M_\odot$ model, and (3) we compare the convective properties of our 3D models to the predictions of Mixing Length Theory (MLT) in three different initial 1D progenitor models.

This paper is organized as follows. In § 2 we describe our computational methods and initial 1D MESA progenitor models. In § 3 we present the results of our 3D simulations including characterizing their global properties, comparing stellar properties to the 1D MESA models, and exploring turbulent entrainment in the O-shell in our 20 $M_\odot$ models. Lastly, in § 4 we summarize our main findings.

2. COMPUTATIONAL METHODS AND INITIAL MODELS

Our methods follow those of Fields & Couch (2020) (referred to as FC20). We draw an initial 1D progenitor for mapping into 3D to simulate the final minutes of Si- and O-shell burning towards iron core-collapse. Here, we highlight the difference in our initial conditions and the initial progenitor set chosen for this study. The MESA inlists, initial and final 1D MESA models, and the four 3D progenitor models produced as a part of this work are publicly available online.

2.1. *1D MESA Stellar Evolution Models*

We employ the stellar evolution toolkit, Modules for Stellar Astrophysics (MESA-revision 12115) (Paxton et al. 2011, 2013, 2015, 2018, 2019), for our spherically-symmetric 1D models. In total, we evolve three solar metallicity, zero-age main-sequence (ZAMS) mass progenitors: $14M_\odot$, $20M_\odot$, and $25M_\odot$. Each progenitor is evolved in MESA from the pre-MS to a time approximately *10 minutes* prior to iron core-collapse. These models utilize temporal/spatial parameters from previous studies shown to provide adequate converge in core quantities at the level of uncertainty due to network size and reaction rates (Farmer et al. 2016; Fields et al. 2018). Our 1D models use the same approximate network as used in FC20, an α-chain network that follows 21 isotopes from ^{1}H to ^{56}Cr (Timmes et al. 2000). Our MESA models are non-rotating and do not include magnetic fields. Mass loss is included using the 'Dutch' wind scheme with an efficiency value of $\eta_{\rm Dutch}$ =0.8. Mixing processes and efficiency values are the same as used in FC20, which use a mixing length parameter of $\alpha_{\rm MLT}$ = 1.5 in all convective regions.

2.2. *3D FLASH Hydrodynamic Stellar Models*

We simulate a total of four 4π 3D hydrodynamic models using the FLASH simulation framework (Fryxell et al. 2000; Dubey et al. 2009). Our models solve the equations of compressible hydrodynamics using the directionally unsplit piecewise parabolic method (PPM), third-order spatial accuracy, solver implemented in FLASH (Lee & Deane 2009). We employ an HLLC Riemann solver (Toro 1999) and use a Courant factor of 0.8. Self gravity is included assuming a monopole ($\ell = 0$) gravitational potential (Couch et al. 2013). Our domain extends to 100,000 km from the origin along an axis in Cartesian geometry utilizing the same boundary

Table 1. Properties of the initial progenitor models at the time of mapping

Initial Mass	$\xi_{2.5}$	$r_{\rm low,Si}$	$r_{\rm high,Si}$	$C_{\rm Si}$	$\mathcal{M}_{\rm rad.,Si}$	$r_{\rm low,O}$	$r_{\rm high,O}$	$C_{\rm O}$	$\mathcal{M}_{\rm rad.,O}$	Simulation Time
($M_\odot$)		(km)	(km)	(g s^{-1})		(km)	(km)	(g s^{-1})		(sec)
14m	0.016	2400	3000	1.2×10^{28}	3.0×10^{-3}	3130	15820	8×10^{27}	1.6×10^{-2}	530.71
20m	0.151	2366	2854	5×10^{27}	1.0×10^{-3}	3120	42000	7×10^{27}	5.0×10^{-3}	643.83
25m	0.519	3700	4150	6×10^{27}	8.0×10^{-4}	5500	44000	5.25×10^{27}	3.2×10^{-3}	606.95

NOTE— 3D FLASH simulation properties of the initial progenitor models at the time of mapping including the initial mass, compactness at a mass coordinate of $m = 2.5$ M$_\odot$, O/Si-shell radial limits, the scaling factor used to produce a 1 or 5% convective velocity profile according to MESA, the resulting radial mach number due to the perturbations, and the total simulation time.

conditions as in FC20. Each model uses adaptive mesh refinement (AMR) with up to eight levels of refinement. We discuss our grid resolution in more detail in § A.

The 3D models are initialized with perturbations in the Si- and O-shell region that are informed by their 1D MESA counterpart at the time of mapping. We use the same notation as in FC20, also used in Müller & Janka (2015) and O'Connor & Couch (2018b). In Table 1 we show properties of our initial progenitor models at the time of mapping into FLASH including the compactness ($\xi_{2.5}$), shell radii, simulation time, perturbation scaling factor C, and the resulting radial mach number ($\mathcal{M}_{\rm rad.} = v_{\rm rad.}/c_{\rm s}$, where $c_{\rm c}$ is the local sound speed) at the start of the simulation caused by the perturbations. The imposed perturbations are performed in the r and θ components of the velocity field with topology determined by spherical harmonic indices and a scaling factor informed by the convective velocity profile of the 1D MESA model.

For the 14 $M_\odot$ model we take the Si-shell region to be at a location of $\approx$ 2400 km to 3000 km within this region, a scaling factor C of 1.2×10^{28} g s^{-1}. The O-shell region is taken to be from $\approx$ 3130 km to 15820 km and we choose a value of C of 8.0×10^{27} g s^{-1}. The locations of the shell regions were determined by the composition profiles and corresponded to radii enclosing the region at which the isotope was the most abundant and had a non-zero convective velocity according to MESA. For the Si-shell, the C value was chosen to represent the average value needed to produce 1% of the convective velocity predicted by MESA. In other words, we compute an approximate scaling factor such that the initial angle-average FLASH convective velocity profile is equal 1% of the mean convective speed in the 1D MESA model in this region. In the O-shell region the value of C was chosen in a similar way except corresponding to 5%. The Si-shell region used spherical harmonic and radial numbers of $n = 1, \ell = 9, m = 5$ while the O-shell region used $n = 1, \ell = 7, m = 5$ (initially larger scale perturbations). The resulting average radial mach number in the Si- and O-shell regions due to these perturbations were $\mathcal{M}_{\rm rad.,Si} \approx 3 \times 10^{-3}$ and $\mathcal{M}_{\rm rad.,O} \approx 1.6 \times 10^{-2}$, respectively. We note that for this model, we observe a weakly burning Ne-shell region at $\approx$ 11000 km. We do not employ separate initial perturbations for this shell. Instead, our O-shell perturbations cover both of these shell regions in radius.

Our 20 M$_\odot$ model was initialized in a similar fashion except the scaling factors chosen for both the Si- and O-shell regions corresponded to a value of 1% of the average value needed to reproduce the convective velocity speeds predicted by MESA. In this model, the Si-shell region is located $\approx$ 2366 km to 2854 km within this region, a scaling factor C of 5.0 $\times 10^{27}$ g s^{-1}. The O-shell region is located at $\approx$ 3120 km to 42000 km and we choose a value of C of 7.0 $\times 10^{27}$ g s^{-1}. For this particular model, a non-convective predominantly silicon region exists between these two regions. This model uses the same perturbation shape parameters. In this model, the initial perturbations produce average radial mach numbers in the Si- and O-shell regions of $\mathcal{M}_{\rm rad.,Si} \approx 1 \times 10^{-3}$ and $\mathcal{M}_{\rm rad.,O} \approx 5 \times 10^{-3}$, respectively. For this particular model, this results in radial velocity speeds of $\approx \pm$ 40 km s^{-1} in the O-shell region with speeds in the Si-shell $\approx \pm$ 20 km s^{-1}

Lastly, the 25M$_\odot$ model has a Si-shell region from $\approx$ 3700 km to 4150 km where we apply a scaling factor of C of 6 $\times 10^{27}$ g s^{-1}. The O-shell region for this model extends from 5500 km to 44000 km where we use an average scale factor of C of 5.25 $\times 10^{27}$ g s^{-1}. Similar to the 20 M$_\odot$ model these scalings were chosen to reproduce approximately 1% of the convective velocity predicted by MESA at the time of mapping. This model uses the same spherical shape parameters as the 20M$_\odot$ model as well. In this model, the perturbations produce mach numbers in the SI- and O-shell regions of $\mathcal{M}_{\rm rad.,Si} \approx 8.0 \times 10^{-4}$ and $\mathcal{M}_{\rm rad.,O} \approx 3.2 \times 10^{-3}$, respectively.

Our FLASH simulations utilize the approximate 21 isotope network (approx21) with the same updated weak reaction rate used for electron capture onto ^{56}Ni from Langanke & Martínez-Pinedo (2000). The Helmholtz stellar equation of state (EoS) as implemented in FLASH is used in all of our 3D simulations (Timmes & Swesty 2000). We do not artificially enhance the total electron capture rates in any simulations presented here. All of our 3D simulations utilize a similar methods as in FC20 where we produce a 2D table from the

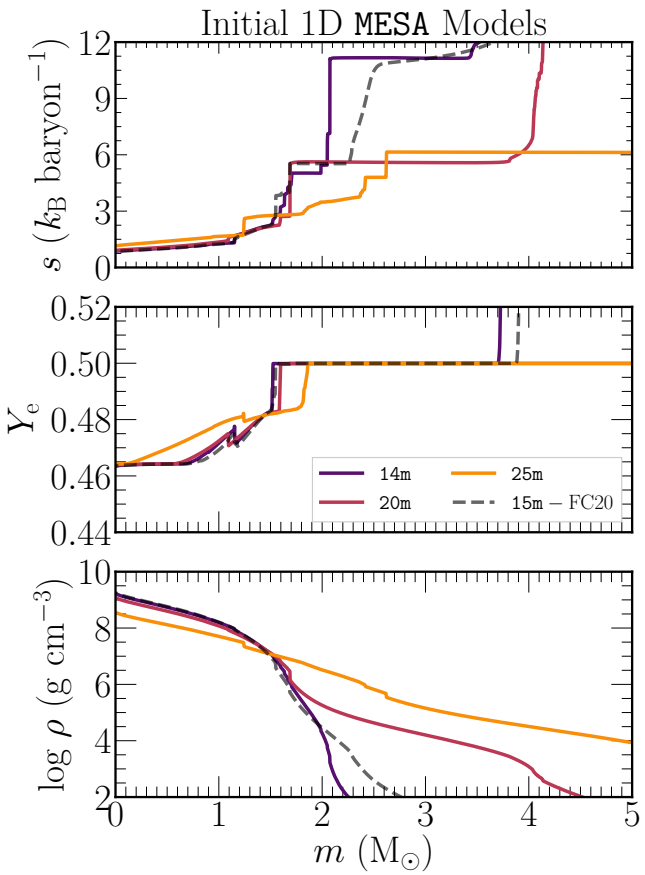

Figure 1. Profiles of the specific entropy (top), electron fraction (middle), and density (bottom) for the three 1D MESA models at time of mapping into FLASH. Also shown is the 15 $M_\odot$ progenitor model from FC20 denoted by the gray dashed line.

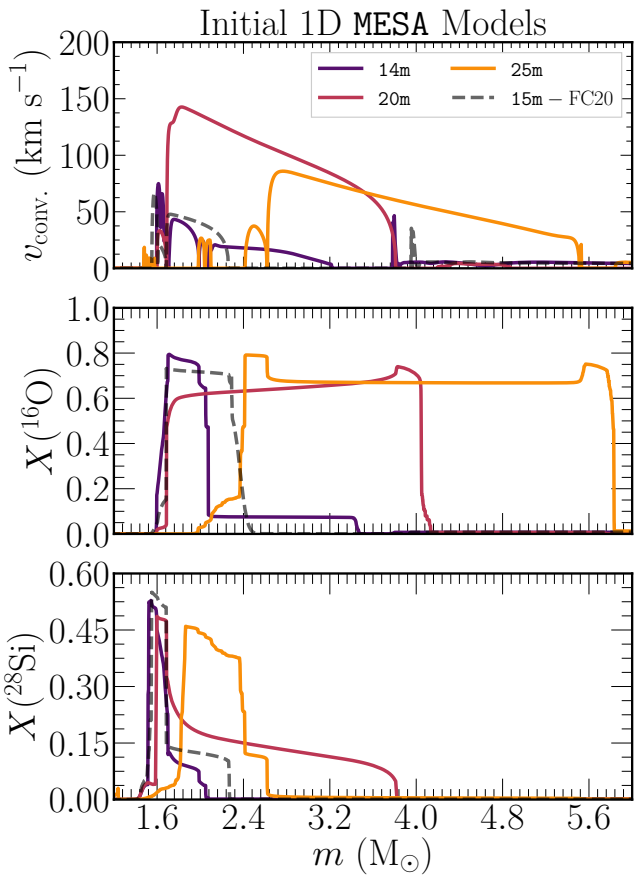

Figure 2. Profiles of the convective velocity (top), oxygen-16 mass fraction (middle), and silicon-28 mass fraction (bottom) for the 1D MESA models at the same time as Figure 1.

MESA profile data for the inner 1000 km from the point of mapping into FLASH until iron core-collapse. Lagrange linear interpolation is then performed in time and radius to obtain a solution FLASH models without the need for a call to the nuclear reaction network. This mapping provides a time-dependent inner boundary condition that ensures the model follows the central evolution of the MESA model but is still significantly below the regions of interest for our study of the multi-D hydrodynamic properties. To help reduce artificial transient during mapping, we use the methods of Zingale et al. (2002) in which we remap the 1D MESA models to a new uniform grid with four times higher resolution than the finest grid spacing. We then alter the density profile to enforce hydrostatic equilibrium (HSE) and close the system with a call to the equation of state.

2.3. *Progenitor Models*

In this study, we aim to explore the range in hydrodynamic properties observed in pre-SN models in their evolution towards iron core-collapse. A metric commonly used to predict the outcome of a pre-SN models is the compactness parameter,

$$\xi_m = \left. \frac{m/M_\odot}{R(M_{\rm bary} = m)/1000\ {\rm km}} \right|_{t=t_{\rm cc}} . \quad (1)$$

This quantity has been used to determine the outcome: explosion vs. implosion, in a range of different progenitors (O'Connor & Ott 2011; Sukhbold et al. 2016). In general, it has been shown that a lower compactness value favors explosion while a higher value $\xi_{2.5} > 0.45$ can result in failed explosion and formation of stellar mass black hole. The compactness parameter has also been shown to correlate with the integrated total neutrino emission count in successfully exploding model (Warren et al. 2020). Models with larger $\xi_{2.5}$ were found to produce more to neutrinos owing to the more massive baryon proto-neutron star (PNS) mass associated to its larger value.

To sample the range of compactness seen in other studies we choose our initial 1D MESA to span a range of values of compactness at time of mapping: $\xi_{2.5} \approx 0.016$, 0.151, and 0.519, for the 14 $M_\odot$, 20 $M_\odot$, and 25 $M_\odot$ models, respectively. For comparison, the 15 $M_\odot$ model of FC20 had a core compactness of $\xi_{2.5} \approx 0.014$. O'Connor & Ott (2011) predict

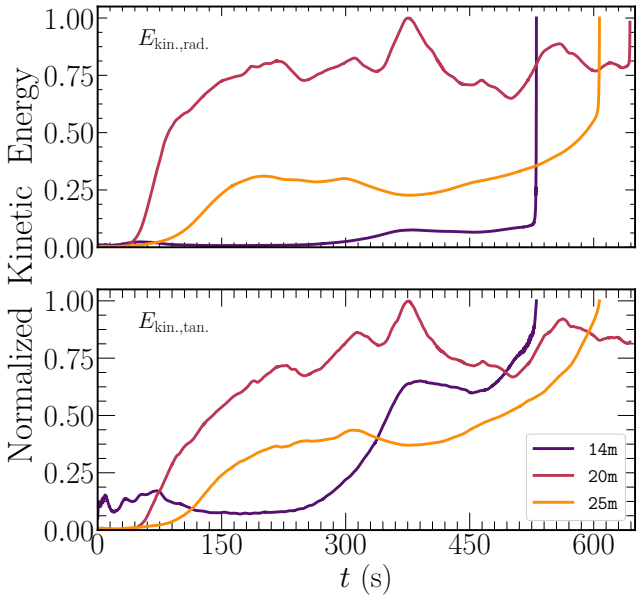

Figure 3. Time evolution of the radial and tangential ($\theta+\phi$) kinetic energy throughout the simulation. For comparison between the different progenitor models, we normalize each simulation to the peak kinetic energy in the simulation.

that models with $\xi_{2.5} \geq 0.45$ such as our 25 $M_\odot$ would fail to explode (assuming a moderately stiff EoS such as LS220 (Lattimer & Swesty 1991)) forming a BH within ≈ 0.5 s post bounce. It should be noted that the core compactness values quoted in Table 1 should be viewed as a lower limit as we measure this quantity at the time of mapping into FLASH and not at core-collapse.

In Figure 1 we show the specific entropy (top), electron fraction (middle), and density (bottom) for the 1D MESA models at time of mapping into FLASH. For comparison, we also plot the 15 $M_\odot$ progenitor from FC20. The 25 $M_\odot$ represents the most shallow density profile likely contributing to its larger compactness value. The 14 $M_\odot$ density is most similar to that of the 15 $M_\odot$ model of FC20. The 20 $M_\odot$ has a density profile whose shallowness is somewhat in between the 14 $M_\odot$ and 25 $M_\odot$ model. This is consistent with the trend seen for the values of compactness for these models.

In Figure 2 we show the convective velocity (top), oxygen-16 mass fraction (middle), and silicon-28 mass fraction (bottom) for the 1D MESA models at the time of mapping into FLASH. The 14 $M_\odot$ and 20 $M_\odot$ models, similar to the 15 $M_\odot$ model from FC20 have a rather narrow Si-shell region. However, in the 25 $M_\odot$ model we see a Si-shell region that spans from $m \approx$ 1.9-2.4$M_\odot$. The 14 $M_\odot$ and 15 $M_\odot$ model have a similar O-shell region width and location. The 20 $M_\odot$ model has a much wider O-shell region that extends from $m \approx$ 1.4-4.0 $M_\odot$. The 25 $M_\odot$ model also has a larger O-shell extending from $m \approx$ 2.4-5.7 $M_\odot$.

The convection speeds as predicted by MESA and mixing length theory (MLT) are largest in the O-shell region for the 20 $M_\odot$ model with $v_{\rm conv.} \approx 120$ km s^{-1}. The 25 $M_\odot$ model shows the second largest speeds with $v_{\rm conv.} \approx 70$ km s^{-1}. The 14 $M_\odot$ and 15 $M_\odot$ model show similar, slower speeds of $v_{\rm conv.} \approx 40$ km s^{-1}. In all of the 1D models (except for the 25 $M_\odot$ model), convection in the Si-shell region show speeds of $v_{\rm conv.} \lesssim 50$ km s^{-1}. The 25 $M_\odot$ model shows slower convective speeds of $v_{\rm conv.} \lesssim 35$ km s^{-1} at the time of mapping.

3. 3D EVOLUTION TO IRON CORE-COLLAPSE IN MULTIPLE PROGENITORS

We evolve a total of four 4π 3D hydrodynamical massive star models for approximately the final 10 minutes up to and including gravitational instability and iron core collapse. Three models with initial masses of 14 $M_\odot$, 20 $M_\odot$, and 25 $M_\odot$ are evolved with velocity fields initialized using the methods and parameters described in § 2. To assess the impact of the initial velocity field topology on our results we also evolve an additional 20 $M_\odot$ model using different spherical harmonic indices but otherwise the same parameters.

Each simulation is evolved up to the simulation time corresponding to iron core collapse as determined by MESA . This time corresponds with that at which the peak infall velocity within the iron core exceeds 1000 km s^{-1}. In the following sections, we explore various aspects of our models including the general properties of three of our models, characterization of their convective shells, and comparisons of the angle-averaged profiles of the 3D simulations to the 1D results from MESA . We explore the impact of the initial perturbations by comparing our two 3D 20 $M_\odot$ models in § 3.4.

3.1. *Global Properties*

In Figure 3 we show the time evolution of the radial and tangential components of the kinetic energy for the three 3D models of varied ZAMS mass. After an initial transient phase, the 14 $M_\odot$ model reaches a quasi-steady state represented by a near constant value of 20% of the local maximum at early times for the total tangential kinetic energy ($\approx 1 \times 10^{46}$ erg) until $t \approx 300$ s. In Figure 4 we show the angle-average tangential velocity and radial Mach number profiles for the 14-$M_\odot$ model at six different times. Beyond 300 s (or ≈ 231 s prior to core-collapse), the convective speeds in the O-shell region increase until a new local maxima in the kinetic energy is found near $t \approx 375$ s. At time $t - t_{\rm CC} = -100$ s (≈ 430 s simulation time), the peak tangential velocity speeds are approximately 160 km s^{-1} throughout the shell with a corresponding total kinetic energy of $E_{\rm kin.} \approx 1 \times 10^{47}$ erg. Assuming a radius for the convective O-shell region of $r_{\rm O} \approx 7500$ km we can compute an approximate convective turnover time of $\tau_{\rm conv.,O} \approx 2r_{\rm O}/v_{\rm tan.,O} \approx 94$ s. The model undergoes undergoes a few convective turnovers

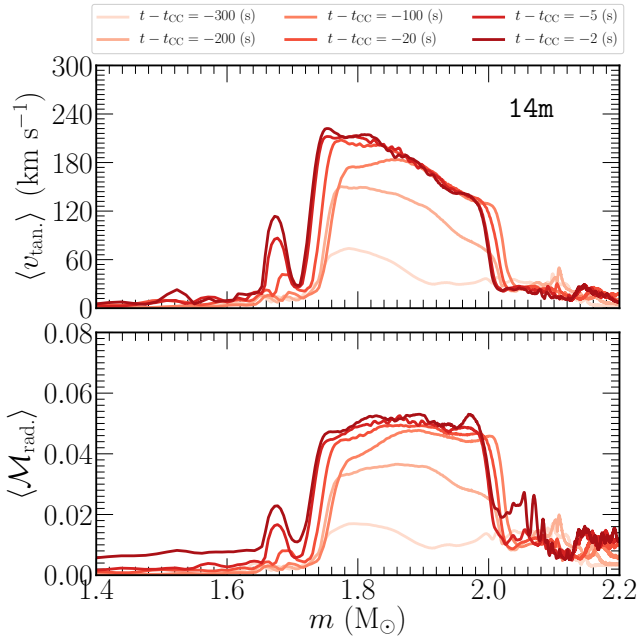

Figure 4. Angle-average profiles of the tangential ($\theta + \phi$) velocity (top) and the radial Mach number (bottom) at six different times for the 14 M$_\odot$ model.

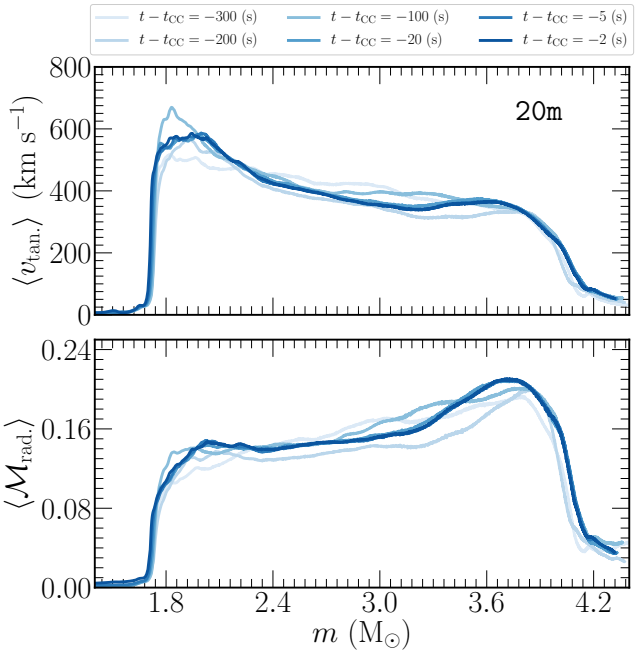

Figure 5. Same as in Figure 4 but for the 20 M$_\odot$ model.

in the O-shell within this new state before core contraction continues to accelerate, increasing the convective speeds further and pushing the model out of equilibrium as collapse ensues.

For the 14-M$_\odot$ model, we observe a radial Mach number (bottom panel of Figure 4, where $\langle ... \rangle$ denotes the angle-average of a particular quantity) of $\mathcal{M}_{rad.} \approx 0.05$ in the O-shell. In the Si-shell region the radial Mach number is $\mathcal{M}_{rad.} \lesssim 0.01$ until the five seconds when a peak value of $\mathcal{M}_{rad.} \approx 0.02$ is reached. FC20 find a similar value in the O-shell of their 15-M$_\odot$ model but a larger value in the Si-shell region than observed here. Both of these models find radial Mach numbers that are about 50% than observed in the O-shell region of the 3D 18 M$_\odot$ model of Müller et al. (2016).

The 20-M$_\odot$ model follows a qualitatively different evolution. For the first $\approx$ 200 s of the simulation, the radial and tangential components of the kinetic energy show a continued increase until reaching a saturation point. At this time, the model maintains a total kinetic energy value of $E_{kin.} \approx 6 \times 10^{48}$ erg. In Figure 5 we show convective velocity and Mach number profile for the 20 M$_\odot$ model. As times as early as $t - t_{CC} = -300$ ($t = \approx 343$ s for the 20-M$_\odot$ model), we observe tangential velocity speeds of $v_{tan.} \approx 450$ km s^{-1} within the O-shell region. Using the O-shell radius, we obtain a convective turnover time of $\tau_{conv.,O} \approx 172$ s. This suggests that our 20-M$_\odot$ model completed approximately three full convective turnovers in the O-shell region. In this simulation, the Si-shell region is thin and experiences only very weak convection. Our discussion will be limited to the O-shell for this model. However, we do find significant mixing at the C/O shell interface in the 20 M$_\odot$ model. The properties of the 20-M$_\odot$ model will be expanded upon and compared to the additional 20-M$_\odot$ model with different velocity field perturbations in § 3.4.

The 20-M$_\odot$ model shows radial Mach values that are much larger than those of our 14-M$_\odot$ model and the models of FC20. In Figure 5 (bottom panel), we find a value of $\mathcal{M}_{rad.} \approx 0.15$ at the base of the convective O-shell ($m \approx 1.8$ M$_\odot$) and $\mathcal{M}_{rad.} \approx 0.21$ at the edge fo the O-shell / C/O shell interface. These values are relatively constant in profile shape and magnitude for the final 300 seconds prior to collapse unlike our 14 M$_\odot$ model which grow in magnitude up to the final seconds prior to collapse.

Our 25 M$_\odot$ model follows an evolutionary path that is different from the other two models. The model reaches about 30% of the peak radial kinetic energy at a time of $t \approx 150$ s. The kinetic energy fluctuates only slightly once reaching this saturated value of total kinetic energy corresponding to a value of $E_{kin.} \approx 1 \times 10^{48}$ erg. In Figure 6 we show convective profiles now for the 25 M$_\odot$ model. We can estimate a convective turnover time for the O-shell utilizing the tangential velocity speeds of $v_{tan.} \approx 240$ km s^{-1} observed from $t \geq 150$. The speeds observed in the convective O-shell region lead to a turnover time of $\tau_{conv.,O} \approx 320$ s. The turnover time in the O-shell region suggests that our model completed one full turnovers from $t \approx 150$ to 500 s. At $t \approx 500$ s and beyond,

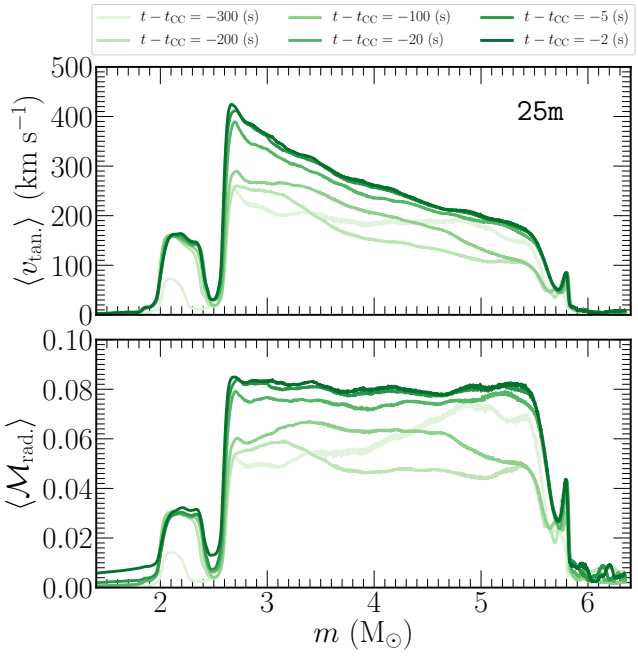

Figure 6. Same as in Figure 4 but for the 25 M$_\odot$ model.

the acceleration of the contracting iron core leads to a gradual increase of both of the components of the kinetic energy relative to their max values at collapse. In this model, we find a larger Si-shell region where convection becomes efficient and relevant to the dynamics of the model near collapse. At $t \approx 300$ s, the width of the Si-shell expands and the convective velocity speeds begin to increase. The speeds in this shell region saturate at a value of $v_{tan.} \approx 160$ km s^{-1} at $t \approx 400$ s, maintaining this value until core-collapse. Within the Si-shell region, we find a convective turnover time of $\tau_{conv.,Si} \approx 6$ s suggesting that from $t \approx 400$ s to core-collapse, our 25 M$_\odot$ captures 34 convective turnovers. The 25 M$_\odot$ model shows radial Mach numbers of $\mathcal{M}_{rad.} \approx 0.03$ in the Si-shell and $\mathcal{M}_{rad.} \approx 0.08$ in the O-shell region in the final 20 seconds prior to collapse.

In Figure 7 we show the a pseudocolor slice plot for the specific ^{28}Si mass fraction (left column), the radial velocity (middle column), and the radial mach number (right column) in the $x-y$ plane at a time approximately 5 seconds before iron core-collapse. The differences between the three simulations are shown here mainly in the relative size of the O-shell regions, convective flow properties, and mixing within the different shell regions.

3.2. *Power Spectrum Of Convective Shells*

To further quantify the convective properties in our 3D models, we decompose the perturbed radial velocity field into spherical harmonics for the O-shell region (and also the Si-shell region for the 25 M$_\odot$ model). Similar to FC20, the total power for a given spherical harmonic order, ℓ, as

$$c_\ell^2 = \sum_{m=-\ell}^{\ell} \left| \int Y_\ell^m(\theta,\phi) v'_{rad.}(r_{Shell},\theta,\phi) d\Omega \right|^2 , \quad (2)$$

where $v'_{rad.} = v_{rad.} - \tilde{v}_{rad.}$, with $\tilde{v}_{rad.}$ corresponding to the mean background radial velocity speed at the chosen shell radius (Schaeffer 2013). In the 14 M$_\odot$, 20 M$_\odot$, and 25 M$_\odot$ models the O-shell regions are evaluated at r_O =5000 km, r_O =5000 km, and r_O =10 000 km, respectively. In the 25 M$_\odot$ model, the Si-shell region is evaluated at r_{Si} =3900 km. The expected dominant mode can be also approximated using

$$\ell = \frac{\pi}{2} \left(\frac{r_+ + r_-}{r_+ - r_-} \right) , \quad (3)$$

where r_+ and r_- are the upper and lower shell radii, respectively (Foglizzo et al. 2006). In Figure 8 we show the resulting O-shell power spectra for three of our 3D models.

The 14 M$_\odot$ model shows a relatively constant power spectrum during the last 100 s prior to collapse, the spectra is peaked at a spherical harmonic index of $\ell = 4$. Before this, at 300 seconds prior to collapse, convective is relatively underdeveloped and power is significantly less across scales. At $t - t_{CC} = -200$ s, the spectrum shows a peak at $\ell = 7$, the driving scale due to our initial perturbations. Energy is then transferred to larger scales at $\ell = 4$ and remains there for the duration of the simulations. As the simulation approaches collapse, we observe a slight increase in power at larger scales $\ell = 1-3$. The dominant mode predicted by using Equation 3 is found to be $\ell \approx 2.38$. The excess in power at $\ell = 4$ is likely attributed to the Cartesian nature of our grid geometry and increased numerical viscosity near the grid axes.

The power spectrum for the 20 M$_\odot$ model (top right of Figure 8) shows a significantly different qualitative evolution towards collapse. At $t - t_{CC} = -200$ s, the power is distributed across many scales with a characteristic peak at $\ell = 2$ suggesting the flow is dominated by a large scale quadrupole flow structure. This results also agrees with Equation 3 which predicts a dominant mode of $\ell \approx 1.82$. A similar dominant mode was observed in the 18 M$_\odot$ model of Müller et al. (2016) in the final moments prior to collapse. At $t - t_{CC} = -100$ s, energy in this mode and the $\ell = 1$ mode increase, with $\ell = 1$ becoming the dominate mode. At later times closer to collapse, the peak at $\ell = 2$ decreases in power with scales of $\ell = 1, 4$ increasing in power. In the final 5 seconds prior to collapse, the dominant mode is observed at $\ell = 1$ with power in intermediate scales of $\ell = 4-8$.

The 25 M$_\odot$ simulation shows a qualitative evolution towards collapse in the convection shell that has traits of the 14 M$_\odot$ and 20 M$_\odot$ models. At early times of $t - t_{CC} = -300$ s and $t - t_{CC} = -200$ s, an excess of power is again observed at an $\ell = 4$ mode suggesting grid aligned artifacts contributing

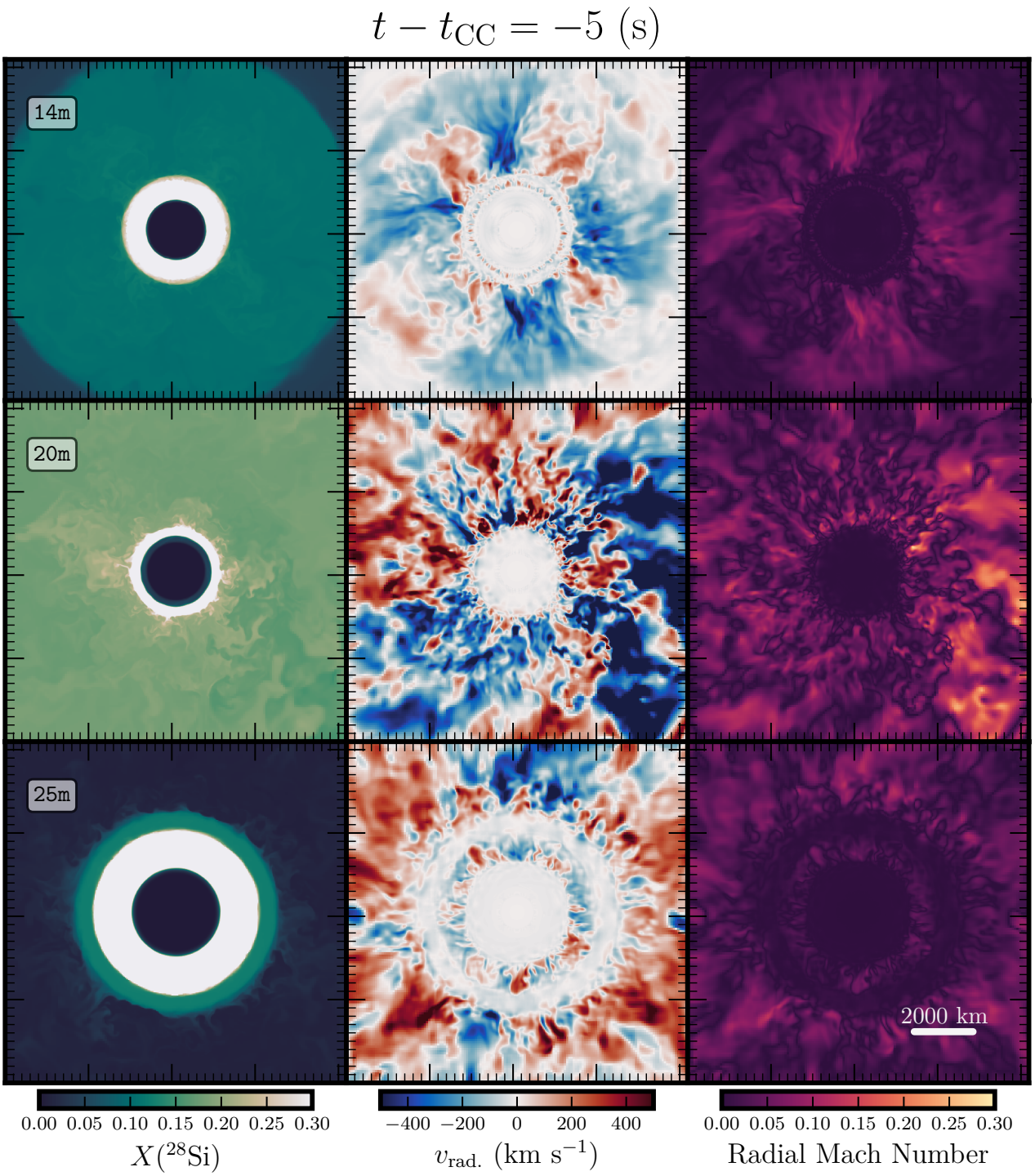

Figure 7. Slice plot for the specific ^{28}Si mass fraction (left column), the radial velocity (middle column), and the radial mach number (right column) in the $x-y$ plane at a time approximately 5 seconds before iron core-collapse for three of our 3D models.

to the power spectrum of the radial velocity field. However, at times beyond this, the 25 $M_\odot$ model shows a reduction in power at this mode with a shift in the peak power contribution occurring at $\ell = 2$. The predicted dominant mode is found to be $\ell \approx 2.01$. The peak spherical harmonic mode remains $\ell = 2$ for the final 100 s of the simulation with a slight contribution at the driving scale ($\ell = 7$) observed in the final 5 seconds before core collapse.

Figure 9 shows the power spectrum of the radial velocity field in the Si-shell region of the 25 $M_\odot$ model at five dif-

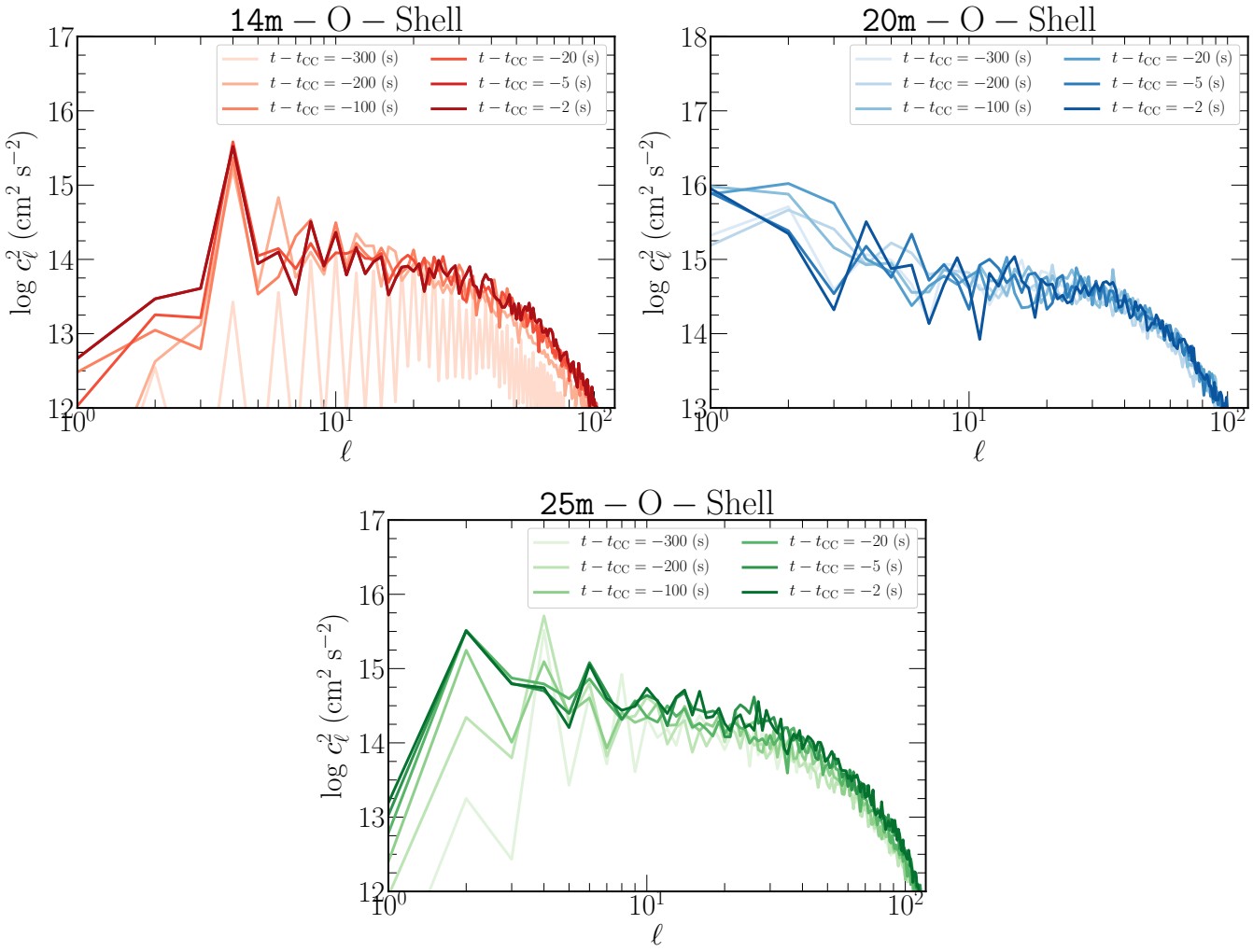

Figure 8. Power spectrum of the radial velocity decomposition in the convective O-shell region for three of the 3D models.

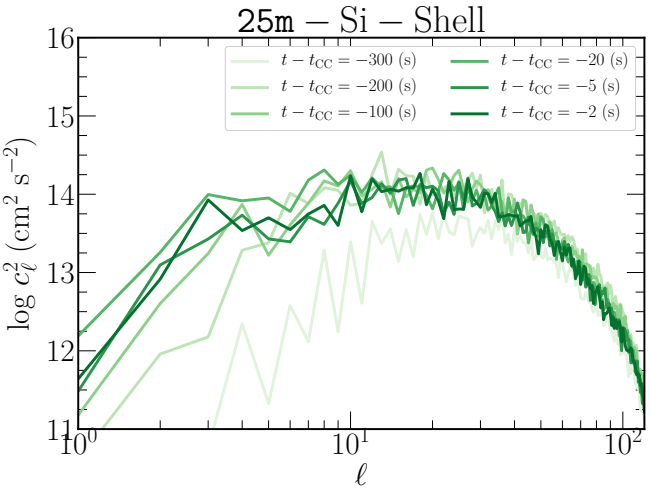

Figure 9. Same as in Figure 8 but for the 25 $M_\odot$ Si-shell region.

ferent times. Overall, the Si-shell region shows less power across scales. Convection begins to contribute to the power spectrum at times beyond 200 s prior to collapse. At this time, the convective Si-shell region has also expanded in radius to allow for a larger scale dominant mode to emerge. Using the approximate shell radii at $t - t_{CC} = -100$ s, we find a predicted dominant mode of $\ell \approx 10.09$. The spectrum at this point is characterized by a broad range of power at intermediate scales from $\approx \ell = 6 - 15$. At later times, we observe a slight increase in power at larger scales near $\ell = 2 - 4$. Five seconds prior to collapse, the dominant modes are found to be found near spherical harmonic indices of $\ell = 15 - 30$.

3.3. *Comparisons with 1D* MESA *models*

An important aspect of our 3D will be their ability to inform 1D MESA models of CCSN progenitors. It was shown in FC20, that the 3D simulations found angle averaged convective speeds that were on the order of *four* times larger than predicted by MESA . Larger non-radial convective velocity speeds in 3D CCSN progenitors than their 1D counterparts have implications that can lead to favorable conditions for explosion. Specifically, increased non-radial convective speeds

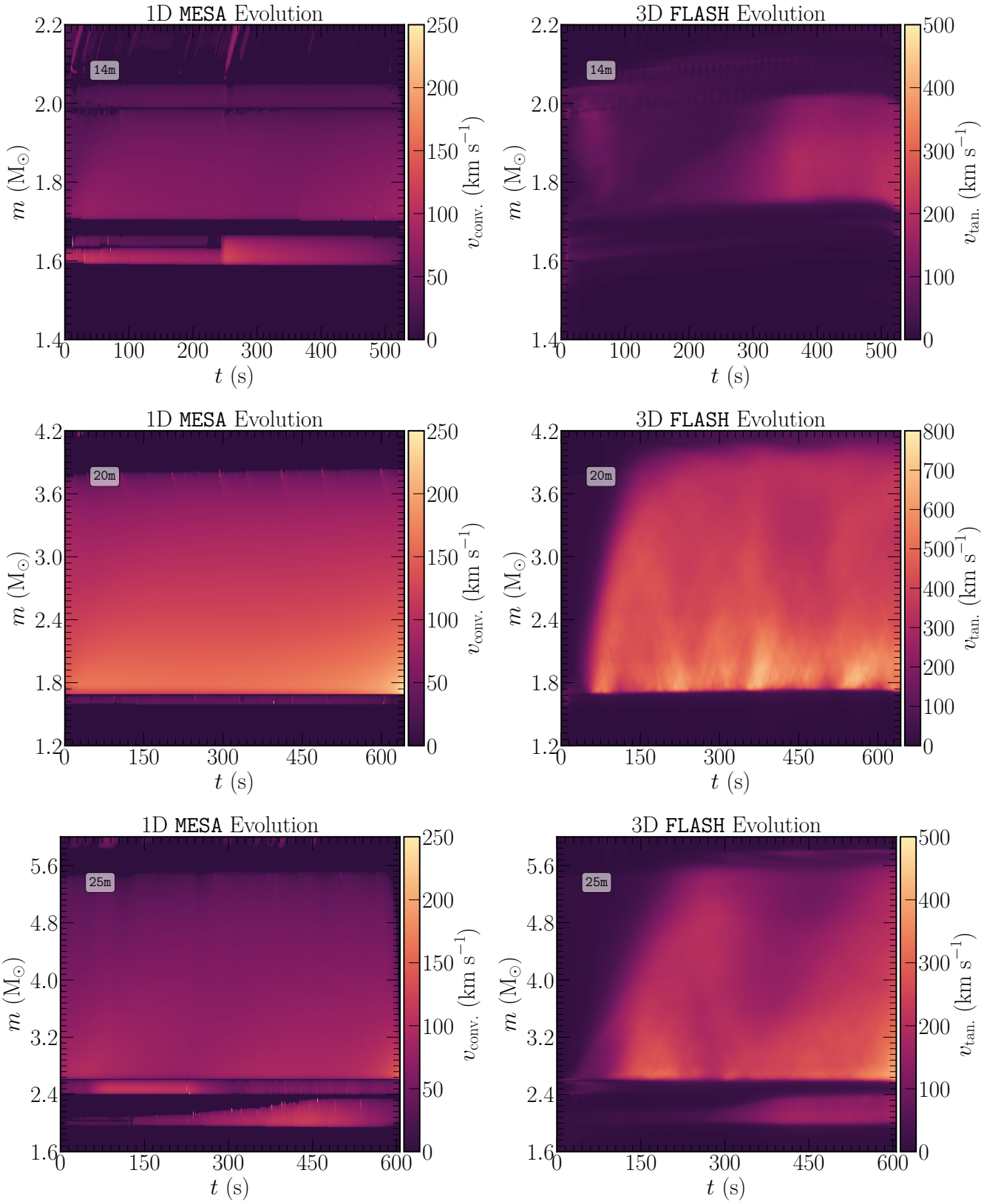

Figure 10. Pseudocolor heatmaps of the convective velocity profiles according to the 1D MESA models (left column) compared the angle-averaged profiles of the tangential velocity component for the three 3D FLASH simulations (right column). In all case, the scale for the 3D simulations is more than twice that of the MESA models for our choice of mixing length parameter of $\alpha_{\rm MLT} = 1.5$.

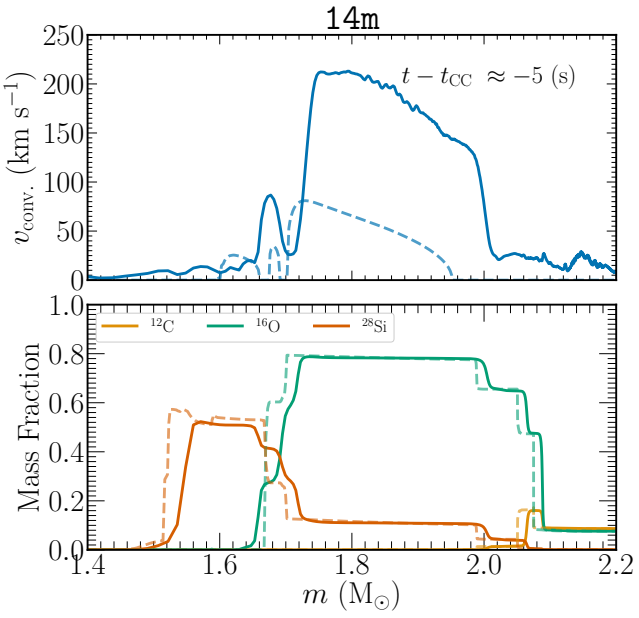

Figure 11. Angle-averged tangential velocity (top) and mass fraction profiles for ^{12}C, ^{16}O, and ^{28}Si compared to the 1D profiles from MESA at a time approximately 5 seconds prior to iron core-collapse. The dashed line in both plots corresponds to the MESA profile and the solid line corresponds to the 3D FLASH simulation.

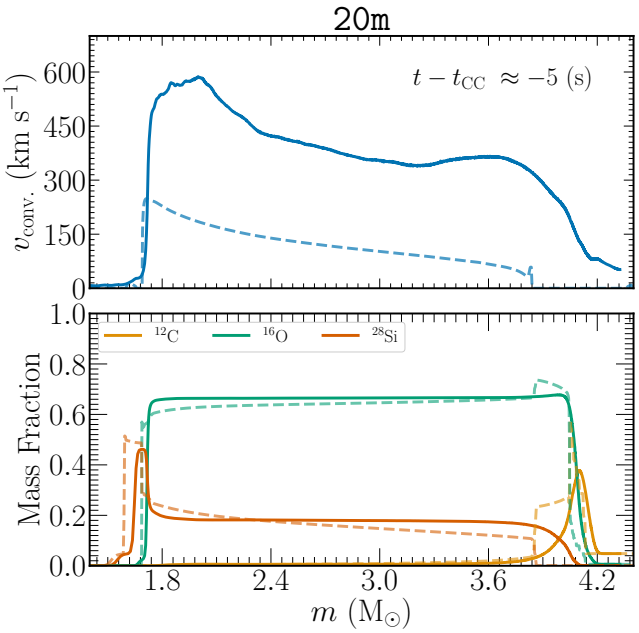

Figure 12. Same as in Figure 11 but for the corresponding 20 M$_\odot$ models.

can work to increase the mass in the gain region which can indirectly alter the effective neutrino heating rates and contribute to greater turbulent stresses in the gain layer (Couch & Ott 2013, 2015). Here, we compare angle-average profiles from our full 4π 3D simulations to their 1D MESA counterparts.

In Figure 10 we show the time evolution of the angle-averaged tangential velocity component for each 3D model (right column) and the time evolution of the corresponding 1D MESA convective velocity profiles predicted by MLT. The angle-average properties are weighted by the corresponding cell mass in each bin. For the profiles used to produce these heat maps we use $N = 2048$ bins and use linear interpolation to smooth the raw profiles. Qualitatively, most of the 3D models agree well with the MESA predictions. The largest differences are found for the 14 M$_\odot$ model where the convective region appears to expand and contract for the first few hundred seconds of the simulation at which point the tangential velocity speeds reach $v_{tan.} \approx$ 200-300 km/s. The extent of the O-shell in the 20 M$_\odot$ model differs somewhat from the MESA model due to mixing at the convective boundary layer between the O- and C-shell regions. This mixing will be examined further in § 3.4. The 25 M$_\odot$ matches the MESA model qualitatively well, where we see a slight expansion of the Si-shell region predicted by MESA also shown in the 3D model at $t \approx 350$ s. In the following subsections, we will explore each 3D model compared to its MESA counterpart in more detail.

3.3.1. *14 M$_\odot$*

In Figure 11 we show the angle-average tangential velocity profile (top) and the specific mass fraction for three major isotopes: ^{12}C, ^{16}O, and ^{28}Si (bottom) for the 3D 14m model approximately five seconds prior to core-collapse. Also shown are the corresponding MESA profiles at the same time before core-collapse denoted by the dashed lines of the same color. For the 14 M$_\odot$ model, we find that a few qualitative features worth mentioning. First, the 1D MESA model shows a peak convective velocity in the O-shell region of $v_{conv.} \approx 50$ km s^{-1}. This value is approximately *four times* smaller than predicted by our 3D tangential velocity profiles where a peak value of velocity is found of $v_{conv.} \approx 210$ km s^{-1}. Beyond this, we observe that the 1D model is more compact with the shell locations closer to the iron core (lower specific mass coordinate). This difference is likely attributed to the slight expansion of the 3D model (See Figure 10, top right).

The mass fraction profiles between the 1D and 3D models are qualitatively similar other than the 3D model being less compact (shells at larger mass coordinate) and the compositional gradients being smoothed at the boundary due to increased mixing. One notable feature in the 3D model is the lack of a Si-rich region at the base of the Si-shell region. The 1D model shows a peak in ^{28}Si from $m \approx$ 1.50-1.54 M$_\odot$. However, in the 3D simulation, we observe instead one merged smoothed Si region. This merged region is able to

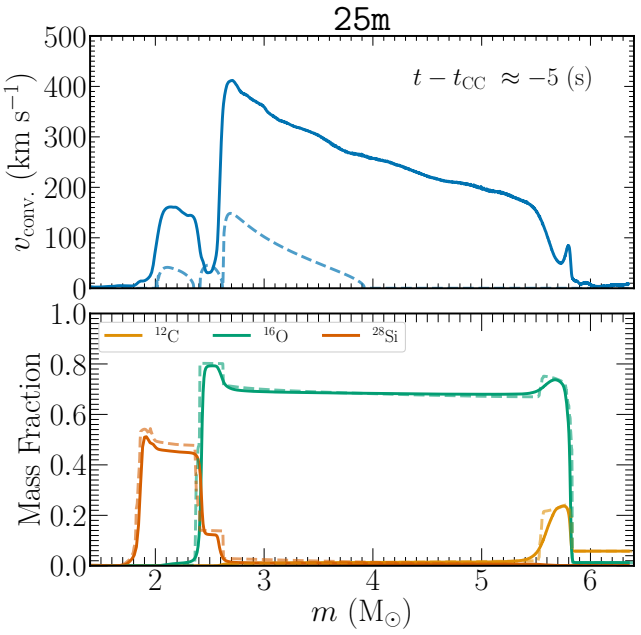

Figure 13. Same as in Figure 11 but for the corresponding 25 M$_\odot$ models.

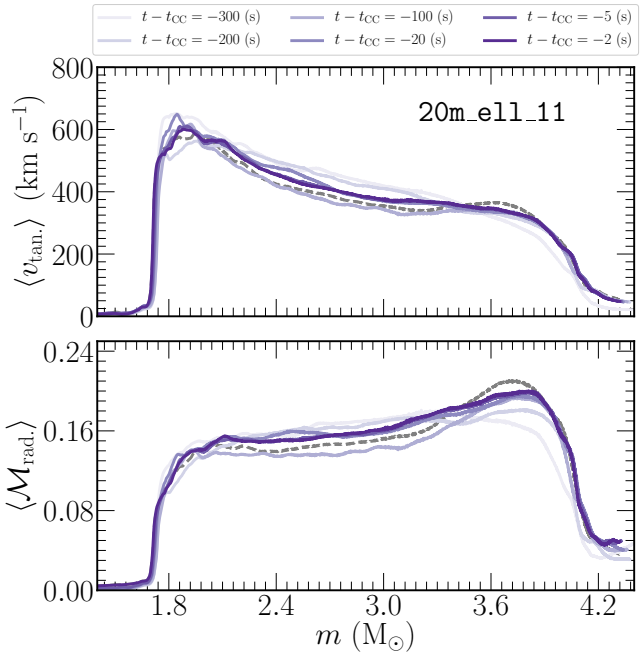

Figure 14. Same as in Figure 4 but for the `20m_ell_11` model. The dashed gray line are the profiles from the `20m` at $t - t_{CC} = -2$ s plotted again here for comparison.

reach higher tangential velocity speeds of $v$conv. $\approx$ 80 km s^{-1} in the 3D model.

3.3.2. *20 $M_\odot$*

Figure 12 shows the convective velocity and mass fraction profiles for the 20 M$_\odot$ 3D and 1D `MESA` models at the same time as in Figure 11. We find that the location of the respective shell locations between 1D and 3D are in better agreement than the 14 M$_\odot$ models which showed a difference of $\Delta M_O \approx 0.02$ M$_\odot$. In the 20 M$_\odot$ models compared here, the location of the base of the O-shell is found at a specific mass coordinate of $m \approx 1.8$M$_\odot$. The extent of the O-shell differs slightly between the two model, likely attributed to the mixing at the boundary between the O- and C-shell regions. The extra mixing at this boundary will be discussed further in § 3.4. Similar to the 14M$_\odot$ model, the convective velocity in the 1D model is less than observed in the 3D simulation. In this particular case, we find speeds three times larger in the 3D model than what is predicted by the 1D `MESA` model. The mass fractions for both models follow similar behavior as the 14 M$_\odot$ models (but with less shell expansion / contraction) in that the profiles are smoothed out and sharp features from the 1D model are not present. One particular case is at the edge of the O-shell region where a slight increase of ^{12}C and ^{16}O from $m \approx$ 3.9-4.2 M$_\odot$ is not observed in the 3D simulation, suggesting it is mixed in or out of the O-shell region during the simulation in 3D.

3.3.3. *25 $M_\odot$*

Lastly, the convective and isotopic mass fractions profiles for the 25-M$_\odot$ models are shown in Figure 13 at $t - t_{CC} = -5$ s. In the 25-M$_\odot$ model, we see similar shell location agreement between the 3D and 1D `MESA` models suggesting less expansion/contraction compared to the 14M$_\odot$ model and the 15M$_\odot$ model of FC20. However, unlike the 20 M$_\odot$ model, and to some degree the 14M$_\odot$ model, the extent of the O-shell region disagrees significantly between the 3D and 1D models. The 3D 25 M$_\odot$ model suggests a convective O-shell region that extends from $m \approx$ 2.5-6.0 M$_\odot$ where and the `MESA` model has the convective speeds going to zero at $m \approx$ 4.0 M$_\odot$. In the bottom panel, the ^{16}O mass fraction profiles agree remarkably aside from the smoothed composition gradients in the 3D profile. We find tangential velocity speeds in the O-shell region that peak at $v_{conv.} \approx 400$ km s^{-1}, a factor of four times larger than predicted by the `MESA` model at the base of the O-shell. Recall that in the Si-shell region of the 1D `MESA` model at this time we see two convective shells with speeds of $v_{conv.} \approx 30$ km s^{-1}. In the 3D model, we observe instead a merged Si-shell with $v_{tan.} \approx 260$ km s^{-1}.

3.4. *A closer look at the 20 $M_\odot$ models*

In order to test the effect of our choice of velocity field initialization methods described in § 2, we explore the results of our additional 3D 20 M$_\odot$ model. This model was evolved using a larger spherical harmonic index for the O-shell ($\ell = 11$) than the fiducial 20-M$_\odot$ model resulting in initially smaller scale perturbations. Otherwise, the quantities used to initial-

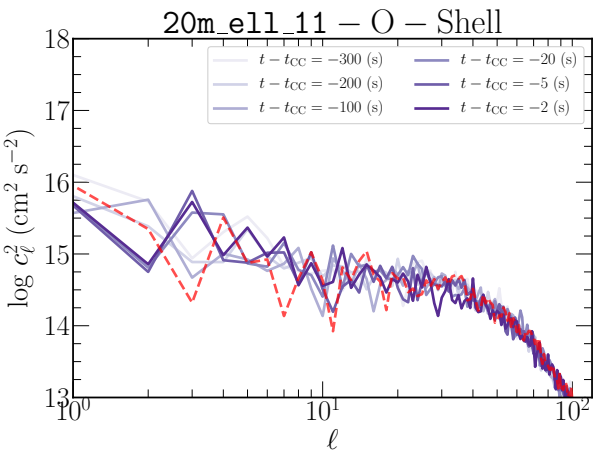

Figure 15. Same as in Figure 8 but for the 20m_ell_11 3D model. Also shown is the spectrum for the 20m model at $t - t_{CC} = -5$ s (red dashed line) for comparison.

ize the velocity field are the same as listed in Table 1 for 20m. We label this additional 3D 20 $M_\odot$ model 20m_ell_11. Figure 14 shows the angle-average tangential velocity and Mach number for this model at six times prior to collapse. Also shown are are the profiles from the 20m plotted again here for comparison via thin dashed lines. The differences between the profiles of the two models are quantitively small. The main differences can be observed near the edge of the O-shell region, $m \approx 3.8$ $M_\odot$ where the 20m model (dashed line) shows a *slightly* larger velocity and radial Mach number than the 20m_ell_11 model. We can more quantitatively explore the differences between these models by considering the power spectrum of the O-shell region.

We compute the power spectrum for the O-shell region for the 20m_ell_11 in Figure 15. For this model, we compute the spectra in the same way as the 20m, taking $r_O = 5000$ km. The spectrum five seconds prior to collapse for the 20m is also shown for comparison (red dashed line). The spectra shown are qualitatively similar except for the 20m_ell_11 model showing the dominant mode to be at $\ell = 3$ near collapse (instead of $\ell = 1$ for the 20m model). At $t - t_{CC} = -5$ c, the 20m model shows slightly more power at $\ell = 1$ and $\ell = 2$ with a deficit of power at $\ell = 3$ compared to the other model. At intermediate scales, the models show relatively similar power.

In Figure 12 we observed smoothing of the ^{12}C chemical stratification in the 3D angle-average profiles that were not observed in MESA . This smoothing suggests additional mixing at the boundary of the convective O-shell region. Instabilities at the convective boundaries can induce mixing described as turbulent entrainment. In the case of O-shell burning, such entrainment can lead to ingestion of C fuel into the O-shell, the likes of which could have implications for the synthesis of odd-Z elements depending on the entrainment rate (Ritter et al. 2018). Turbulent entrainment has been studies previously in 3D simulations of convection O-shell burning (Meakin & Arnett 2007; Müller et al. 2016; Andrassy et al. 2020). Here, we explore the mixing at the boundary of the C/O shell regions and the dependence of these results on our choice of initial perturbations in our two 20 $M_\odot$ models.

We can define the bulk Richardson number as a measure of the relative stiffness of the C/O shell boundary. Using a form of the equation that relates the convective scale length to that of the pressure scale height we can define the bulk Richardson number as

$$R_B = \frac{\delta\rho}{\rho} \frac{P}{\rho v_{conv.}^2}, \quad (4)$$

where $\delta\rho/\rho$ corresponds to the density contrast across the boundary and $v_{conv.}$ refers to the turbulent velocity components perpendicular to the boundary. For the 20m model we use $\delta\rho/\rho \approx 0.22$ and an convective velocity of $v_{conv.} \approx 320$ km s^{-1} near the boundary, both computed using angle-average profiles of the relevant quantity. Using these values we find a dimensionless bulk Richardson number of $R_B \approx 37$. This result suggests a relatively "soft" boundary that is slightly more stiff than the 18 $M_\odot$ model seen in Müller et al. (2016) and similar to the core convection boundary in Meakin & Arnett (2007). The 20m_ell_11 model only shows a slight difference with $R_B \approx 41$.

We show slice plots of the ^{12}C mass fraction for both 3D models at three different times near collapse in Figure 16. Both models show relatively similar distributions of ^{12}C at $t = 300$ s primarily influenced by the interaction of the initial velocity field produced by our perturbations and the shell boundary. The subsequent aspherical deformation of this boundary begins to diverge between the two models due to the different drive scale ℓ that characterizes the velocity field. Qualitatively, 20m shows a larger fraction of ^{12}C being pulled down in the northern hemisphere of the slice of model. The bottom panel suggest that less ^{12}C is being entrained and that this is potentially linked to the choice of ℓ in the initialization of the velocity field.

To explore this more quantitatively, we compute the mass of the convective O-shell as a function of time for both models. In Figure 17 we show the approximate mass of the convective O-shell region for both of our 20 $M_\odot$ 3D models. We define this to be the mass enclosed between an angle-average specific entropy of $s = [3.6, 6.1]$ k_B baryon^{-1} When considering the temporal evolution of the mass of the convective O-shell, we can observe the same divergence in the mass at times greater than $t \approx 240$ s. Beyond this point, the mass increases at a faster rate than the other 20 $M_\odot$ model before reaching a saturation point at $t \approx 375$ s, where both models follow a similar slope. In the last ≈ 100 s, the 20m model

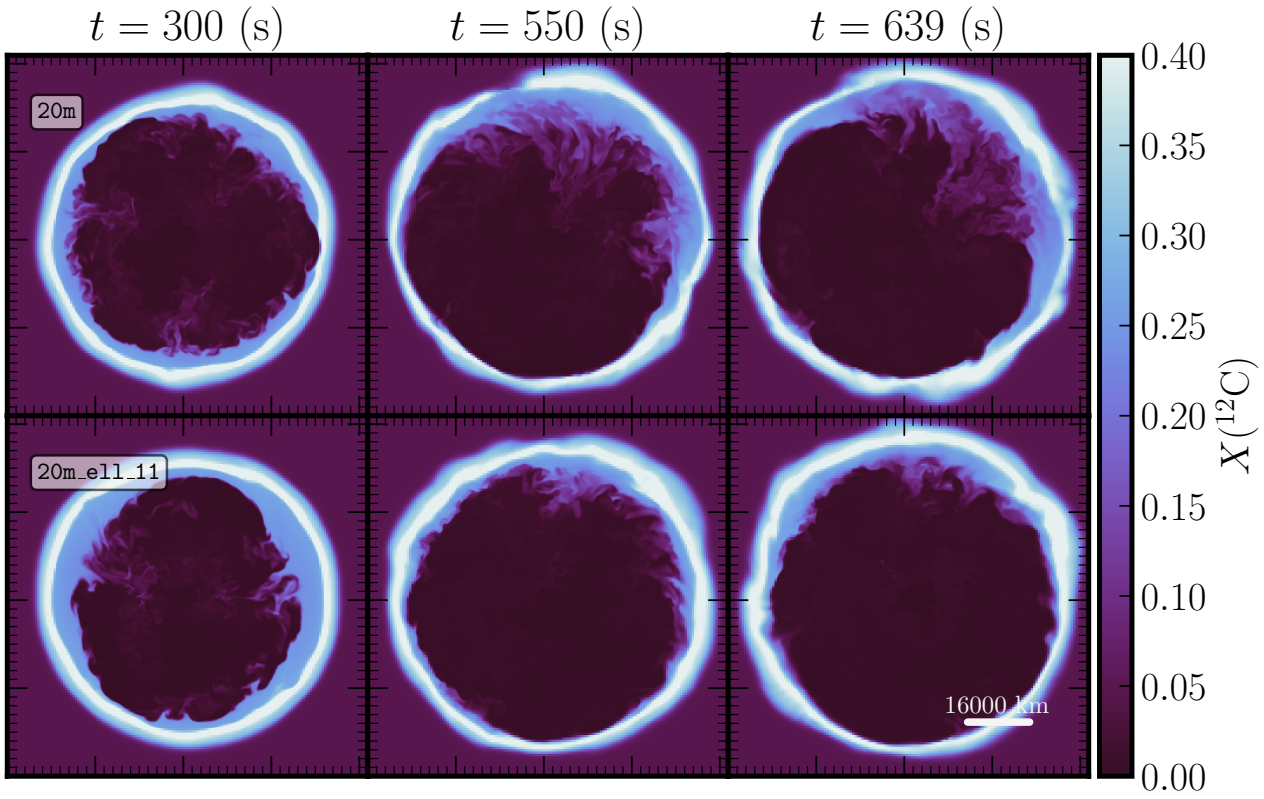

Figure 16. Slice in the $x-z$ plane of the ^{12}C mass fraction for the two 3D 20 $M_\odot$ models at t = 300 s, t = 550 s, and t = 639 s (5 seconds before collapse) from left to right, respectively.

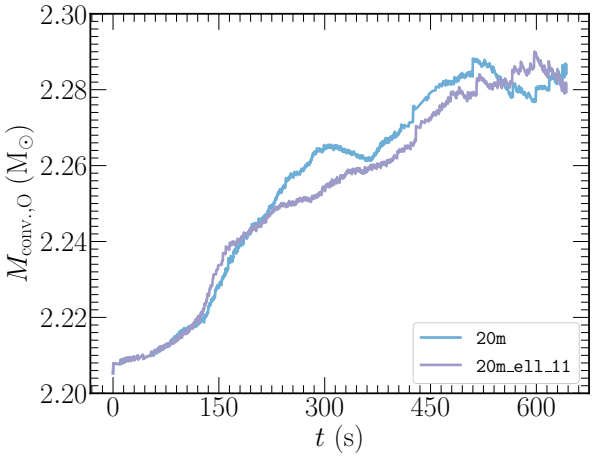

Figure 17. Mass of the convective O-shell region as a function of time for the `20m` and `20m_ell_11` models.

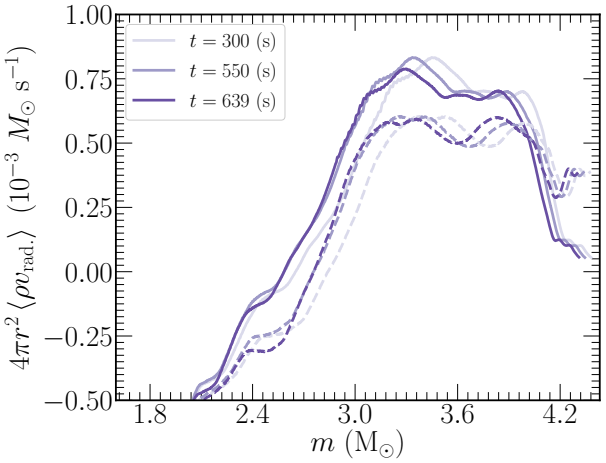

Figure 18. Turbulent mass flux as a function of specific mass coordinate for the two 3D 20 $M_\odot$ models (model `20m_ell_11` is shown by the dashed lines) at t = 300, 550, and 639 s. The approximate location of the C/O interface corresponds to a specific mass coordinate of $m \approx 4$ $M_\odot$.

shows a slight decrease in mass due to the deformation of the edge of the O-shell leading to fluctuations in the average shell radius.

In Figure 18 we show mass flux in the O-shell region of our 20 $M_\odot$ models (model `20m_ell_11` is shown by the dashed lines) at t = 300, 550, and 639 s. In the `20m` model we observe a positive flux at the boundary of the C/O shell region ($m \approx 4$ $M_\odot$) of 7.5 $\times$ 10^{-4} $M_\odot$ s^{-1}. The `20m_ell_11`

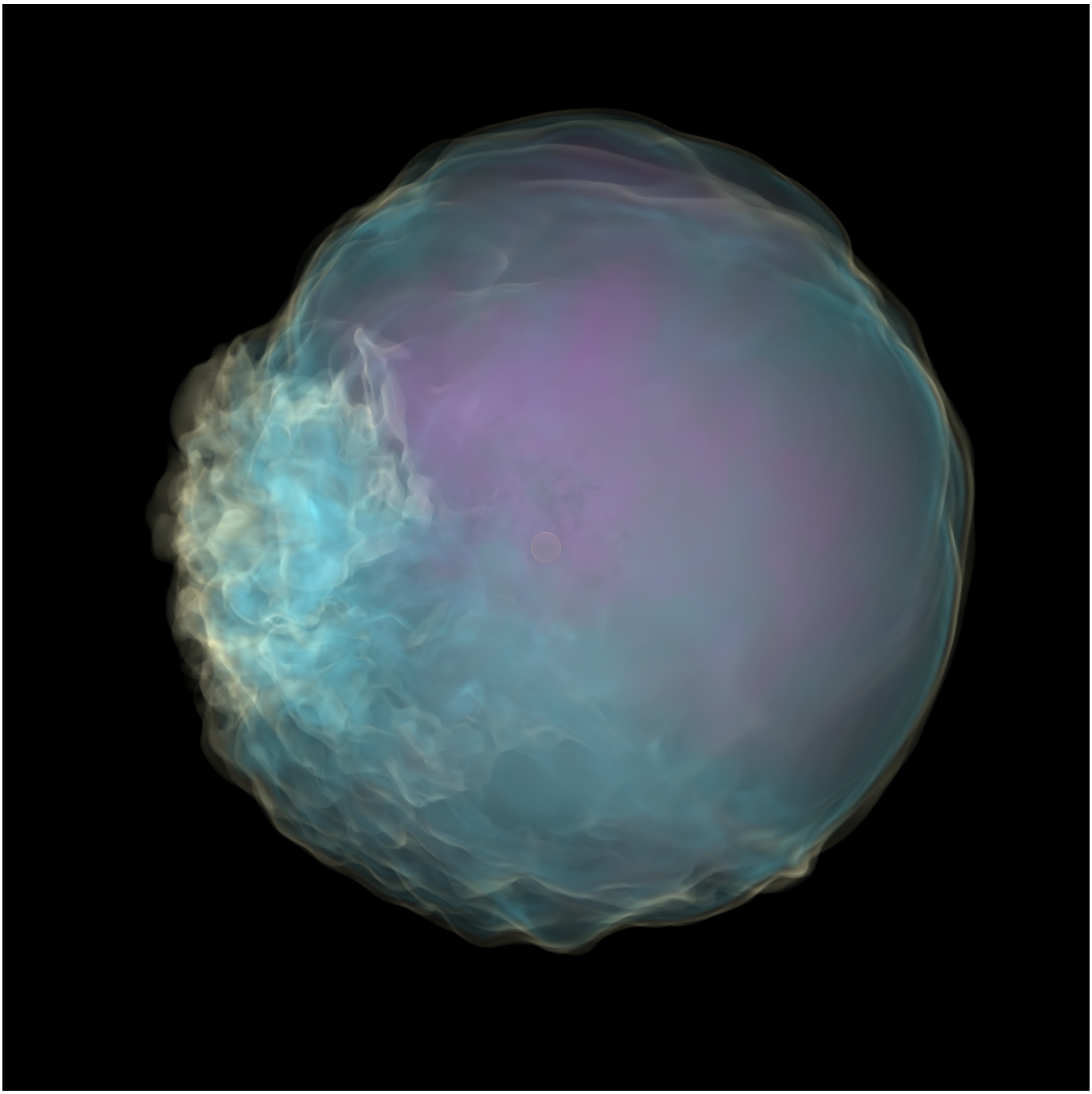

Figure 19. Volume rendering of the ^{28}Si mass fraction for the `20m` model at t = 639 s. The transfer function consists of three Gaussian peaks to highlight the low (yellow, 0.05), moderate (blue, 0.1), and high (purple, 0.2) concentration of Si. The low concentration regions highlight fresh ^{12}C fuel being mixed down into the O-shell region. The blue region trace the approximate extent and structure of the convective O-shell region. Purple regions follow high concentrations of fresh Si being mixed due to O-shell burning. The iron core at this point spans an approximate radius of $r \approx 2520$ km and is shown in gold at the center of the model. The O-shell at this time spans a radius of $r \approx 60\,000$ km. This visualization was produced using `yt` and the colormap library `cmocean`.

model shows a *slightly* less efficient mass entrainment 5.2 $\times$ 10^{-4} $M_\odot$ s^{-1}. Despite having a more stiff boundary between the C/O shell regions in our simulations, we observe a larger rate of mass entrainment than found in Müller et al. (2016). Our results also suggest that the characteristic properties of the velocity field initialization can lead to slight differences in the net mass entrainment rate as observed in our two 20 $M_\odot$ simulations. Larger scale initial perturbations can lead

to more significant deformation of the overlying C-shell region which can enhance (potentially artificially) the ingested ^{12}C into the O-shell region. In Figure 19 we show a volume rendering of the ^{28}Si mass fraction for the `20m` model at $t = 639$ s. The yellow and blue regions trace the low and moderate concentration of ^{28}Si. These regions trace mixing of the ^{12}C into the O-shell region. The iron core is shown by a gold spherical contour with a sharp peak Gaussian at an approximate entropy $s = 4\ k_B$ baryon^{-1}.

4. SUMMARY AND DISCUSSION

We have presented 3D hydrodynamic simulations of O- and Si-shell burning in massive star models using `MESA` and the `FLASH` simulation framework. We follow up to the final ten minutes prior to core-collapse to capture the development of the turbulent convective flow prior to and including gravitational collapse. In this study, we considered initial 1D progenitor models of 14-, 20-, and 25 $M_\odot$ to survey a range of O/Si shell density and compositional configurations. We also evolved an additional 3D 20 $M_\odot$ model to investigate the impact of our choice of initial velocity perturbations.

In our 14 $M_\odot$ model, we observed relatively weak O-shell convection with the peak of the power spectrum near a spherical harmonic index of $\ell = 4$. We also observed a slight increase in power at larger scales $\ell = 1-3$ near collapse for this model. The convective O-shell region showed radial Mach numbers of $\mathcal{M}_{\rm rad.} \approx 0.05$ near collapse. Despite weaker convection compared to our other 3D models, we found that angle-average convective velocity profile was approximately four times larger than the speeds predicted by `MESA` in the moments prior to collapse for our choice of mixing length parameters.

Our baseline `20m` model showed the most energetic power spectrum in the O-shell region with power residing at the largest scales of $\ell = 1-3$ near collapse. The convective velocity profile showed speeds *three* times larger than the 1D `MESA` model counterpart. We also simulated an additional 20 $M_\odot$ model with a different initial velocity field topology in the O-shell to explore the impact of our initiial conditions. When choosing an initially smaller scale ($\ell = 11$ instead of $\ell = 7$) velocity field topology we observed variations in the amount of turbulent entrainment of ^{12}C at the C/O shell interface. The model with smaller scale topology for the O-shell velocity field (model `20_ell_11`) showed a reduced positive turbulent mass flux at the C/O interface and an overall less efficient mass entrainment rate of 5.2×10^{-4} $M_\odot$ s^{-1} near collapse. This value was found to be about ≈ 31 % less than the baseline 20 $M_\odot$ model (using $\ell = 7$) which showed prominent large-scale mixing at the boundary leading to additional C-ingestion at a time $t - t_{CC} = -300$ s. Both of our 3D 20 $M_\odot$ models found Mach numbers of $\mathcal{M}_{\rm rad.} \approx 0.15-0.20$ in the convective O-shell region maintained throughout the final 300 seconds prior to collapse.

The results of our 25 $M_\odot$ showed qualitatively properties similar to the 14- and 20 $M_\odot$ model. At early times, the power spectrum shows a peak near $\ell = 4$. However, at later times, energy is transferred towards larger scales with the bulk of energy at $\ell = 1-3$ near collapse. In this model, the convectively active Si-shell region can be characterized by power over a broad range of intermediate scales of $\ell = 10-20$ as the simulation approaches collapse. This model showed radial Mach numbers of $\mathcal{M}_{\rm rad.} \approx 0.03$ and $\mathcal{M}_{\rm rad.} \approx 0.08$ in the Si- and O-shell regions in the seconds prior to collapse, respectively.

The results of the 3D simulations presented in this work show a discrepancy between angle-average profiles of the convective velocities and the 1D `MESA` convection profiles for our choice of input mixing length parameters. This discrepancy has been seen in previous studies. In Jones et al. (2017) they performed simulations of idealized 4π 3D O-shell burning of a 25$M_\odot$ model. The results of this study showed that the convective velocities in the MLT framework, when using diffusion coefficients computed from the angle-average 3D data, can agree within a factor of a few compared to predictions by MLT and the 1D `MESA` model. Work by Herwig et al. (2006) found convective speeds predicted by MLT were a few factors slower than their 2D hydrodynamic simulations of He-flash convection. The discrepancies presented here can be attributed in part to the fact that the convective and burning timescales become similar in the moments leading towards collapse. MLT assumes that the convective mixing happens on the local dynamical timescale and is much shorter than other relevant timescales. Moreover, MLT is assumes a mixing length over which an average velocity is computed, as opposed to a range of convective *time-dependent* scales in the radial and transverse directions as presented in the 3D models of this work. Efforts to provide a new formulation that takes these assumptions and other aspects of turbulent convection into account for a new 1D prescription of stellar convection has been considered in Arnett et al. (2015). Improvements to MLT have also been proposed (Canuto & Mazzitelli 1991; Trampedach et al. 2014).

Recent work by Yoshida et al. (2021) explore the final minutes prior to collapse in 3D simulations of Si- and O-shell burning in 22$M_\odot$ and 27$M_\odot$ progenitors. In their models, they observe peak spherical harmonic modes of $\ell_{\rm peak} = 2-3$ and find that the Mach number can exceed 0.1. These results agree in general with the values found for our 20$M_\odot$ and 25$M_\odot$ models. Except for the case of the radial Mach number of the 25$M_\odot$ model where we find that the peak value near collapse is only found to be ≈ 0.08. They also observe episodic burning burning of O and Ne which lead to an increase in the turbulent mixing found in their simulations.

Similar episodic burning was found in the 18.88 $M_\odot$ model of Yadav et al. (2019). We find no evidence of episodic burning in any of our four 3D simulations.

The set of models presented in this work are a step forward in efforts to produce realistic 3D pre-supernova models that capture the properties of massive stars in their final moments prior to collapse. A key component not yet discussed in this paper is the effect of rotation and magnetism. Recent work by Müller & Varma (2020) suggests that pre-SN models with slow to moderately rotating cores near collapse could play a role in the delayed neutrino-driven mechanism of CCSNe. Efforts towards addressing the impact of magnetic fields in 3D simulations of O-shell burning were performed recently for a 18 $M_\odot$ model, although this model did not include the effect of rotation (Varma & Müller 2021). Rotation and magnetism must be considered in realistic 3D progenitor models as their inclusion is relevant to magnetically-driven (Mösta et al. 2015; Fryer et al. 2019) and ordinary neutrino-driven CCSN explosions (Curtis et al. 2020; Barker et al. 2021) and the multi-messenger signals they produce (Warren et al. 2020; Pajkos et al. 2021).

Software: `MESA` (Paxton et al. 2011, 2013, 2015, 2018, http://mesa.sourceforge.net), `FLASH` (Fryxell et al. 2000, http://flash.uchicago.edu/site/), `yt` (Turk et al. 2011, https://yt-project.org), and `matplotlib` (Hunter 2007, https://matplotlib.org).

ACKNOWLEDGMENTS

We thank Josh Dolence, Sam Jones, Brian O'Shea, and P. N. Sagan, for useful discussions. C.E.F. acknowledges support from the National Science Foundation Graduate Research Fellowship Program under grant number DGE1424871. Research presented in this article was supported by the Laboratory Directed Research and Development program of Los Alamos National Laboratory under project number 20210808PRD1. S.M.C. is supported by the U.S. Department of Energy, Office of Science, Office of Nuclear Physics, Early Career Research Program under Award Number DE-SC0015904. This material is based upon work supported by the U.S. Department of Energy, Office of Science, Office of Advanced Scientific Computing Research and Office of Nuclear Physics, Scientific Discovery through Advanced Computing (SciDAC) program under Award Number DE- SC0017955. This research was supported by the Exascale Computing Project (17-SC-20-SC), a collaborative effort of the U.S. Department of Energy Office of Science and the National Nuclear Security Administration. This work was supported in part by Michigan State University through computational resources provided by the Institute for Cyber-Enabled Research. This research made extensive use of the SAO/NASA Astrophysics Data System (ADS).

APPENDIX

A. `FLASH` SIMULATION RESOLUTION

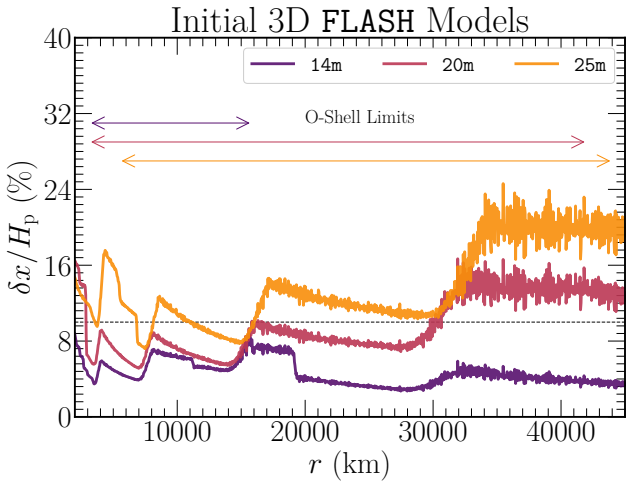

Figure 20. The angle-average cell resolution as a percentage of the relative pressure scale height for the three 3D models at $t = 0$. Also shown are the approximate O-shell radial limits. The dashed horizontal line corresponds to 10% of the pressure scale height.

The finest level of refinement for each model results in a grid spacing of ≈ 32.5 km. The approximate effective resolution for each model varies due to their different initial shell configurations. For the 14 $M_\odot$ model, the finest resolution level is situated at the center of the simulation and extends out to a radius of $r \approx 3500$ km. This region includes the entire iron core and Si-shell resulting in an average resolution of ≈ 8 % of the local pressure scale height, $H_\mathrm{p} = P/\rho G$. The resolution decreases beyond this radius by a factor of two out to $r \approx 7100$ km. In this region, our simulation has a resolution that equates to $\approx 7\%$ H_p. The resolution continues to decrease beyond this radius based based on logarithmic changes in specific density, pressure, and velocity. After initialization, the location of the refinement levels do not change throughout the simulation. The 20 $M_\odot$ model has a qualitatively similar grid with the finest resolution level containing the entire iron and Si-shell region. In the 25 $M_\odot$, model, the finest refinement level extends out to $r \approx 4100$ km. Unlike the other models, in the 25 $M_\odot$ model, this only encompasses the iron core and a portion of the Si-shell region. Within this finest refinement level, the resulting resolution equates to an average of $\approx 5\% H_\mathrm{p}$. Beyond this radius, the grid resolution is decreased by a factor of two but the simulation maintains an approximate effective resolution of $\approx 5\% H_\mathrm{p}$ out to $r \approx 8100$ km. The remainder of the grid resolution is similar to the other two models. In Figure 20 we show the average cell reolution as a percentage of the pressure scale height according to the 3D models. Also shown are the approximate O-shell radial limits for each model.

REFERENCES

Andrassy, R., Herwig, F., Woodward, P., & Ritter, C. 2020, MNRAS, 491, 972, doi: 10.1093/mnras/stz2952

Arnett, W. D., Meakin, C., Viallet, M., et al. 2015, ApJ, 809, 30, doi: 10.1088/0004-637X/809/1/30

Barker, B. L., Harris, C. E., Warren, M. L., O'Connor, E. P., & Couch, S. M. 2021, arXiv e-prints, arXiv:2102.01118. https://arxiv.org/abs/2102.01118

Burrows, A., Radice, D., Vartanyan, D., et al. 2020, MNRAS, 491, 2715, doi: 10.1093/mnras/stz3223

Canuto, V. M., & Mazzitelli, I. 1991, ApJ, 370, 295, doi: 10.1086/169815

Couch, S. M., Chatzopoulos, E., Arnett, W. D., & Timmes, F. X. 2015, ApJL, 808, L21, doi: 10.1088/2041-8205/808/1/L21

Couch, S. M., Graziani, C., & Flocke, N. 2013, ApJ, 778, 181, doi: 10.1088/0004-637X/778/2/181

Couch, S. M., & Ott, C. D. 2013, ApJL, 778, L7, doi: 10.1088/2041-8205/778/1/L7

—. 2015, ApJ, 799, 5, doi: 10.1088/0004-637X/799/1/5

Curtis, S., Wolfe, N., Fröhlich, C., et al. 2020, arXiv e-prints, arXiv:2008.05498. https://arxiv.org/abs/2008.05498

Dubey, A., Antypas, K., Ganapathy, M. K., et al. 2009, Parallel Computing, 35, 512 , doi: https://doi.org/10.1016/j.parco.2009.08.001

Farmer, R., Fields, C. E., Petermann, I., et al. 2016, ApJS, 227, 22, doi: 10.3847/1538-4365/227/2/22

Fields, C. E., & Couch, S. M. 2020, ApJ, 901, 33, doi: 10.3847/1538-4357/abada7

Fields, C. E., Timmes, F. X., Farmer, R., et al. 2018, ApJS, 234, 19, doi: 10.3847/1538-4365/aaa29b

Foglizzo, T., Scheck, L., & Janka, H. T. 2006, ApJ, 652, 1436, doi: 10.1086/508443

Fryer, C. L., Lloyd-Ronning, N., Wollaeger, R., et al. 2019, European Physical Journal A, 55, 132, doi: 10.1140/epja/i2019-12818-y

Fryxell, B., Olson, K., Ricker, P., et al. 2000, ApJS, 131, 273, doi: 10.1086/317361

Herwig, F., Freytag, B., Hueckstaedt, R. M., & Timmes, F. X. 2006, ApJ, 642, 1057, doi: 10.1086/501119

Hunter, J. D. 2007, Computing In Science & Engineering, 9, 90

Jones, S., Andrassy, R., Sandalski, S., et al. 2017, MNRAS, 465, 2991, doi: 10.1093/mnras/stw2783

Langanke, K., & Martínez-Pinedo, G. 2000, Nuclear Physics A, 673, 481, doi: 10.1016/S0375-9474(00)00131-7

Lattimer, J. M., & Swesty, D. F. 1991, NuPhA, 535, 331, doi: 10.1016/0375-9474(91)90452-C

Lee, D., & Deane, A. E. 2009, Journal of Computational Physics, 228, 952 , doi: https://doi.org/10.1016/j.jcp.2008.08.026

Meakin, C. A., & Arnett, D. 2007, ApJ, 667, 448

Mösta, P., Ott, C. D., Radice, D., et al. 2015, Nature, 528, 376, doi: 10.1038/nature15755

Müller, B., & Janka, H. T. 2015, MNRAS, 448, 2141, doi: 10.1093/mnras/stv101

Müller, B., Melson, T., Heger, A., & Janka, H.-T. 2017, MNRAS, 472, 491

Müller, B., & Varma, V. 2020, MNRAS, 498, L109, doi: 10.1093/mnrasl/slaa137

Müller, B., Viallet, M., Heger, A., & Janka, H.-T. 2016, ArXiv e-prints. https://arxiv.org/abs/1605.01393

O'Connor, E., & Ott, C. D. 2011, ApJ, 730, 70, doi: 10.1088/0004-637X/730/2/70

O'Connor, E. P., & Couch, S. M. 2018a, ApJ, 865, 81, doi: 10.3847/1538-4357/aadcf7

—. 2018b, ApJ, 854, 63, doi: 10.3847/1538-4357/aaa893

Pajkos, M. A., Warren, M. L., Couch, S. M., O'Connor, E. P., & Pan, K.-C. 2021, ApJ, 914, 80, doi: 10.3847/1538-4357/abfb65

Paxton, B., Bildsten, L., Dotter, A., et al. 2011, ApJS, 192, 3, doi: 10.1088/0067-0049/192/1/3

Paxton, B., Cantiello, M., Arras, P., et al. 2013, ApJS, 208, 4, doi: 10.1088/0067-0049/208/1/4

Paxton, B., Marchant, P., Schwab, J., et al. 2015, ApJS, 220, 15, doi: 10.1088/0067-0049/220/1/15

Paxton, B., Schwab, J., Bauer, E. B., et al. 2018, ApJS, 234, 34, doi: 10.3847/1538-4365/aaa5a8

Paxton, B., Smolec, R., Gautschy, A., et al. 2019, arXiv e-prints. https://arxiv.org/abs/1903.01426

Pejcha, O., & Thompson, T. A. 2015, ApJ, 801, 90, doi: 10.1088/0004-637X/801/2/90

Ritter, C., Andrassy, R., Côté, B., et al. 2018, MNRAS, 474, L1, doi: 10.1093/mnrasl/slx126

Schaeffer, N. 2013, Geochemistry, Geophysics, Geosystems, 14, 751, doi: 10.1002/ggge.20071

Sukhbold, T., Ertl, T., Woosley, S. E., Brown, J. M., & Janka, H.-T. 2016, ApJ, 821, 38, doi: 10.3847/0004-637X/821/1/38

Timmes, F. X., Hoffman, R. D., & Woosley, S. E. 2000, ApJS, 129, 377

Timmes, F. X., & Swesty, F. D. 2000, ApJS, 126, 501

Toro, E. F. 1999, Riemann Solvers and Numerical Methods for Fluid Dynamics (Springer, Berlin, Heidelberg)

Trampedach, R., Stein, R. F., Christensen-Dalsgaard, J., Nordlund, Å., & Asplund, M. 2014, MNRAS, 445, 4366, doi: 10.1093/mnras/stu2084

Turk, M. J., Smith, B. D., Oishi, J. S., et al. 2011, ApJS, 192, 9, doi: 10.1088/0067-0049/192/1/9

Varma, V., & Müller, B. 2021, arXiv e-prints, arXiv:2101.00213. https://arxiv.org/abs/2101.00213

Warren, M. L., Couch, S. M., O'Connor, E. P., & Morozova, V. 2020, The Astrophysical Journal, 898, 139, doi: 10.3847/1538-4357/ab97b7

Yadav, N., Müller, B., Janka, H. T., Melson, T., & Heger, A. 2019, arXiv e-prints, arXiv:1905.04378. https://arxiv.org/abs/1905.04378

Yoshida, T., Takiwaki, T., Kotake, K., et al. 2019, The Astrophysical Journal, 881, 16, doi: 10.3847/1538-4357/ab2b9d

Yoshida, T., Takiwaki, T., Kotake, K., et al. 2021, ApJ, 908, 44, doi: 10.3847/1538-4357/abd3a3

Zingale, M., Dursi, L. J., ZuHone, J., et al. 2002, ApJS, 143, 539, doi: 10.1086/342754